

# In situ fully vectorial tomography and pupil function retrieval of tightly focused fields

Received: 23 September 2024

Accepted: 3 April 2025

Published online: 11 April 2025



Xin Liu<sup>1,2</sup>, Shijie Tu<sup>1</sup>, Yiwen Hu<sup>1</sup>, Yifan Peng<sup>2</sup>, Yubing Han<sup>1</sup>,  
Cuifang Kuang<sup>1,3</sup>, Xu Liu<sup>1,3</sup>✉ & Xiang Hao<sup>1,3</sup>✉

Tightly focused optical fields are essential in nano-optics, but their applications have been limited by the challenges of accurate yet efficient characterization. In this article, we develop an in situ method for reconstructing the fully vectorial information of tightly focused fields in 3D space, while simultaneously retrieving the pupil functions. Our approach encodes these fields using phase-modulated focusing and polarization-split detection, followed by decoding through an algorithm based on least-sampling matrix-based Fourier transform and analytically derived gradient. We further employ a focus scanning strategy. When combined with our decoding algorithm, this strategy mitigates the imperfections in the detection path. This approach requires only 10 frames of 2D measurements to realize approximately 90% accuracy in tomography and pupil function retrieval within 10 s. Thus, it serves as a robust and convenient tool for the precise characterization and optimization of light at the nanoscale. We apply this technique to fully vectorial field manipulation, adaptive-optics-assisted nanoscopy, and addressing mixed-state problems.

Paraxial beams behave like transverse waves with two-dimensional (2D) polarization orthogonal to the propagation axis. However, when tightly focused by high numerical-aperture (NA) objectives, they always exhibit an evident polarization component along the propagation direction<sup>1–3</sup>, resulting in a 3D polarization structure. More specifically, tightly focused fields refer to the ones formed by focusing a paraxial beam from the laser source onto the sample with a high-NA objective, rather than wide-field illumination or those collected from the sample. These fields play a crucial role in studying light behavior at nanometer scales, such as spin-to-orbital angular momentum conversion<sup>4,5</sup> and topological photonics<sup>6–8</sup>. It also underpins various applications like optical tweezers<sup>9,10</sup>, laser manufacturing<sup>11</sup>, spectroscopy<sup>12</sup>, and point-scanning optical nanoscopy<sup>13,14</sup>. To fully harness its potential, it is vital to accurately and comprehensively characterize these fields, i.e., to capture the fully vectorial information—both the amplitude and phase of all three polarization components. Meanwhile, knowing the pupil function defined on the objective's back focal plane (BFP) is critical for

manipulating and optimizing these fields in experiments. Unfortunately, achieving both aims has been challenging due to the absence of appropriate tools.

Recent advancements have attempted to measure the tightly focused fields through direct magnification<sup>15–18</sup>. It is also feasible to use a probe to detect the near field<sup>19</sup> or map it to the far field<sup>20,21</sup>. However, these methods face limitations due to imperfections in the detection path and require complicated setups. In addition, the far-field mapping needs to capture thousands of images for reconstruction, which are especially time-consuming<sup>21,22</sup>. These techniques are further constrained as they are only available in a 2D plane near the focus, with the 3D reconstruction unrealized. Moreover, the in situ characterization of the associated pupil functions remains unexplored.

To solve these problems, we introduce an approach for reconstructing both the fully vectorial information of tightly focused fields in 3D space and the associated pupil functions using optical encoding and algorithmic decoding. Specifically, the vectorial information is encoded in 2D point spread functions (PSFs) via active phase

<sup>1</sup>State Key Laboratory of Extreme Photonics and Instrumentation, College of Optical Science and Engineering, Zhejiang University, Hangzhou, China.

<sup>2</sup>Department of Electrical and Electronic Engineering, The University of Hong Kong, Hong Kong SAR, China. <sup>3</sup>ZJU-Hangzhou Global Scientific and Technological Innovation Center, Hangzhou, China. ✉e-mail: [liuxu@zju.edu.cn](mailto:liuxu@zju.edu.cn); [haox@zju.edu.cn](mailto:haox@zju.edu.cn)

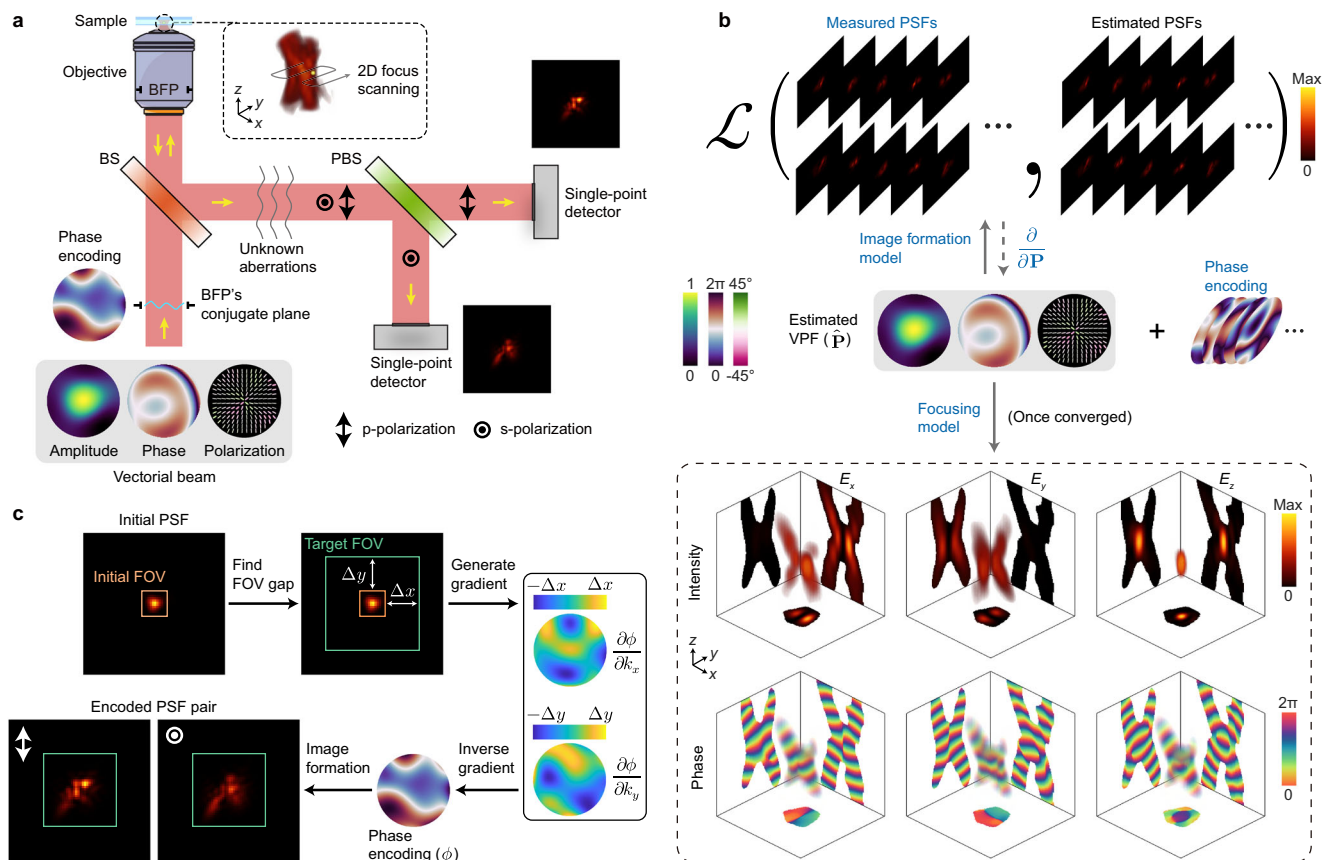


**Fig. 1 | Concept of in situ fully vectorial tomography and pupil function retrieval.** **a** Schematic of optical encoding. The phase encoding is applied on the conjugate plane of the objective's BFP. Yellow arrows indicate the direction of light propagation. Abbreviations: BFP, back focal plane; BS, beamsplitter; PBS, polarizing beamsplitter. **b** Schematic of algorithmic decoding. Blue text represents known parameters or operators. Gray solid and dashed arrows indicate the forward process and the update of the VPF, respectively. The polarization's colormap illustrates

the ellipticity. **c** Phase encoding design. We first define the boundary (orange box) of a pre-captured PSF and the target field of view (FOV) (green box) that encloses the encoded PSF. The gap between the two boundaries correlates with the phase gradient's magnitude of the VPF. We randomly generate the phase gradient within this magnitude constraint, and then derive the phase by computing its inverse gradient. Applying this phase encoding yields the encoded two-channel PSFs within the target FOV. Further details are available in the Methods section.

modulation and polarization-split detection. The information is subsequently decoded using Fourier-transform-based analytical gradient descent. By employing focus scanning to detect the PSFs and leveraging our decoding algorithm, we mitigate the imperfections in the detection path, enabling in situ tomography and pupil function retrieval.

## Principle

Our method reconstructs the tightly focused field ( $\text{PSF}_{\text{vec}}$ ) in 3D space and the corresponding vectorial pupil function (VPF) from several measured 2D PSFs. The whole process is to solve a phase-retrieval problem<sup>23–27</sup>. However, phase retrieval is ill-posed, because different complex fields can produce identical measurements. The challenge is more profound in  $\text{PSF}_{\text{vec}}$  reconstruction due to the inclusion of polarization, especially since the three polarization components are interconnected by the VPF. To eliminate this ambiguity, we implement a joint focusing and detection encoding strategy (Fig. 1a). In detail, we apply phase diversity as the focusing encoding<sup>28,29</sup>, where extra phase modulation with prior knowledge is introduced to VPF, thereby redistributing the  $\text{PSF}_{\text{vec}}$ . Unlike phase diversity realized by defocus or vanilla random modulation<sup>27,28,30</sup>, we elaborately design these phases to balance diversity with signal-to-noise ratio (SNR) (Fig. 1c). This balance is important because complicated VPFs compromise the SNR by over-distorting the PSF, whereas simple ones can not provide enough diversity to support the reconstruction. On the detection side, the PSFs

are acquired by scanning a dipole-like probe, e.g., a gold nanosphere, and collecting the backscattered signal using single-point detectors. While phase diversity typically ensures unique solutions in scalar case<sup>29,31</sup>, the diversity can be unnoticeable when incorporating polarization, rendering the solution ambiguous again under limited SNR conditions. To mitigate this, we separately detect the p- and s-polarization components (Supplementary Section 1). The polarization separation helps decouple the contributions of each 3D polarization component. To support subsequent algorithmic decoding, we establish a comprehensive image formation model for the entire process (Supplementary Section 2).

Given the known phase encoding and the measured PSFs from two polarization channels, we algorithmically retrieve the VPF by solving the following inverse problem:

$$\text{argmin}_{\mathbf{P}} \mathcal{L} \left\{ \mathbb{I}(\mathbf{P}, \Psi), \tilde{\mathbb{I}} \right\}, \quad (1)$$

where  $\Psi$  represents the known phases for encoding, while  $\mathbb{I}$  and  $\tilde{\mathbb{I}}$  are the estimated and measured PSFs, respectively. The error function  $\mathcal{L}$  quantifies the difference between the estimated and measured PSFs, with  $\mathbf{P}$  denoting the estimated VPF. To solve Eq. (1), we develop an algorithm leveraging Fourier transform and analytically derived gradients (Supplementary Sections 3.1–3.2). Once the VPF is obtained, the  $\text{PSF}_{\text{vec}}$  in 3D space can be computed according to the focusing model (Fig. 1b).

Our method provides three major advantages over previous works<sup>15–21</sup>:

- Fully vectorial tomography and pupil function retrieval: The joint focusing and detection encoding strategy enables unambiguous retrieval of the VPF. With the reconstructed VPF, we achieve the fully vectorial tomography of the  $\text{PSF}_{\text{vec}}$  following the focusing model.
- In situ characterization: The focus scanning strategy directly probes the  $\text{PSF}_{\text{vec}}$  near the focus without re-imaging. The single-point detector enables us to record the total energy collected by the objective rather than pixelated images for each scanning point. Therefore, it minimizes the impact of imperfections in the detection path, including amplitude, phase, and polarization aberrations<sup>32</sup>. Besides the benefits of the hardware, our decoding algorithm eliminates imperfections by incorporating them into optimization, further enhancing the method's in situ capabilities.
- High efficiency: Also benefiting from the optical encoding, only several 2D PSF acquisitions are required for accurate reconstruction. Moreover, during algorithmic decoding, we determine the least samples of the VPF and  $\text{PSF}_{\text{vec}}$ , and use matrix-based Fourier transform<sup>33,34</sup> to ensure accurate results with minimal computational effort.

See Supplementary Sections 3.3–3.5 for further details.

## Results

### Simulations

To quantify the performance of our method, we first define the reconstruction accuracy based on normalized root-mean-square-error (Supplementary Section 4.1). Specifically, this metric evaluates the pixel-wise difference between the reconstructed tightly focused fields and the ground truth (in simulations) or the measurements (in experiments). It will be also employed to quantify the accuracy of field manipulation. Following this definition, we began with validating our method through simulations. Various tightly focused beams were successfully reconstructed at approximately 90% accuracy without failure case, including those highly ambiguous ones once our encoding strategy is not applied. Moreover, we also achieved around 80% accuracy even when the background noise is comparable to the signal. Notably, our decoding algorithm allows completing the reconstruction within 10 s on a standard commercial computer. Both in simulations and subsequent experiments, we employed 10 phases for encoding, determined based on the available SNR in our experiments (Supplementary Section 4.3). Additionally, we determined an average peak intensity with 300 photons for the measured PSFs (120-nm pixel size) suffices for the reconstruction. Further details, including the accuracy definition, image processing, the influence of the number of phase encoding and the SNR, and the reconstructed results, are available in Supplementary Section 4. This supplementary section also details the comparison between our method and earlier studies.

### Experiments

Following the simulations are the experimental validations. As direct experimental ground truth is unattainable, we alternatively confirmed the accuracy of the reconstructed results in two ways. First, we compared the amplitude and polarization of the reconstructed VPFs with those measured by a Stokes camera conjugate to the objective's BFP (Supplementary Section 5.1). Second, we used the reconstructed  $\text{PSF}_{\text{vec}}$  to predict the two-channel PSFs at different depths without phase encoding, and then compared them with the measured counterparts that did not contribute to the reconstruction. Notably, the VPFs measured by the Stokes camera only serve as a rough reference, as it is affected by the optical elements before the focus. In contrast, our reconstructed VPFs represent the effective

counterparts that have included these effects. Moreover, compared to VPFs measured by the Stokes camera, the measured two-channel PSFs without phase encoding serve as a precise reference since the detection path remains the same as that for measuring phase-encoded PSFs. More experimental details can be found in the Methods section.

In our experiments, we utilized a vortex half-wave plate (VHWP) to generate two cylindrical vector beams with radial and azimuthal polarization, respectively. These beams are ideal for validating 3D polarization reconstruction because the longitudinal component in their  $\text{PSF}_{\text{vec}}$  is either dominant (for radial polarization) or negligible (for azimuthal polarization)<sup>35</sup>. Initially, we verified our method and corrected phase aberrations in the focusing path with linearly polarized light. The linear polarization (either p- or s-polarization) is less affected by polarization aberrations from optical elements<sup>32</sup>, making the reference VPF more reliable (Supplementary Section 5.2). Following this initial validation and aberration correction, we reconstructed the  $\text{PSF}_{\text{vec}}$  and VPFs of the tightly focused cylindrical vector beams. Figure 2 presents the results. In detail, the reconstructed VPFs generally match the reference ones (Fig. 2a, c), including polarization singularities. Nevertheless, there are some noticeable discrepancies. Specifically, the amplitudes exhibit low-pass filtering due to the FOV limitation of the PSFs. The phases show some variations that ideally should be zero. These discrepancies are mainly attributed to the noise in measured PSFs and VPFs' polarization singularities, with additional phase aberrations potentially introduced by the VHWP after initial aberration correction. Other deviations in the VPFs are dominated by optical elements prior to the focus.

Despite discrepancies in the VPFs, the key features of the  $\text{PSF}_{\text{vec}}$  for cylindrical vector beams are well preserved. For the radially polarized beam, the  $\text{PSF}_{\text{vec}}$  exhibits nearly orthogonal shapes of  $E_x$  and  $E_y$  with a linear dark region and a phase step. Additionally, the longitudinal component  $E_z$  is stronger than the lateral components and exhibits a circularly symmetric intensity and phase around the optical axis. In contrast, although the tightly focused azimuthally polarized beam also shows orthogonal shapes of the lateral components, the longitudinal component is much weaker (ideally zero). In both cases,  $E_y$  is stronger than  $E_x$ , which should ideally be equal. This is due to greater attenuation of the x-component of the VPFs' polarization compared to the y-component, as evidenced by the circular asymmetry of the VPFs' amplitude. Furthermore, the estimated PSFs with phase encoding align well with the measurements (Supplementary Section 5.3), confirming the efficacy of our image formation model and decoding algorithm. Next, we used the reconstructed  $\text{PSF}_{\text{vec}}$  to predict the measured two-channel PSFs without phase encoding, which, as mentioned before, serves as the precise ruler. Notably, in both cases, the predicted PSFs perfectly align with the measured ones at various depths (Fig. 2b, d), reaching around 90% accuracy which is consistent with the simulations. Our prediction is further supported by reconstructing a tightly focused double helix beam, whose PSF has two rotating lobes, and the angle of rotation depends on the axial position (Supplementary Section 5.5).

In these experimental validations, we have incorporated the imperfections of the detection path into the decoding process. The efficacy has been indicated by the reconstruction accuracy. To further illustrate the robustness of our detection strategy in the presence of aberrations, we introduced artificial aberrations by inserting a diffuser into the optical setup (Supplementary Section 5.6). Specifically, when the diffuser was placed in the focusing path, it dramatically distorted the detected PSFs due to induced aberrations. In contrast, when the diffuser was in the detection path, the shape of detected PSFs remained stable despite a decrease in signal strength. This indicates that our detection strategy is robust against aberrations, which is crucial for in situ characterization.

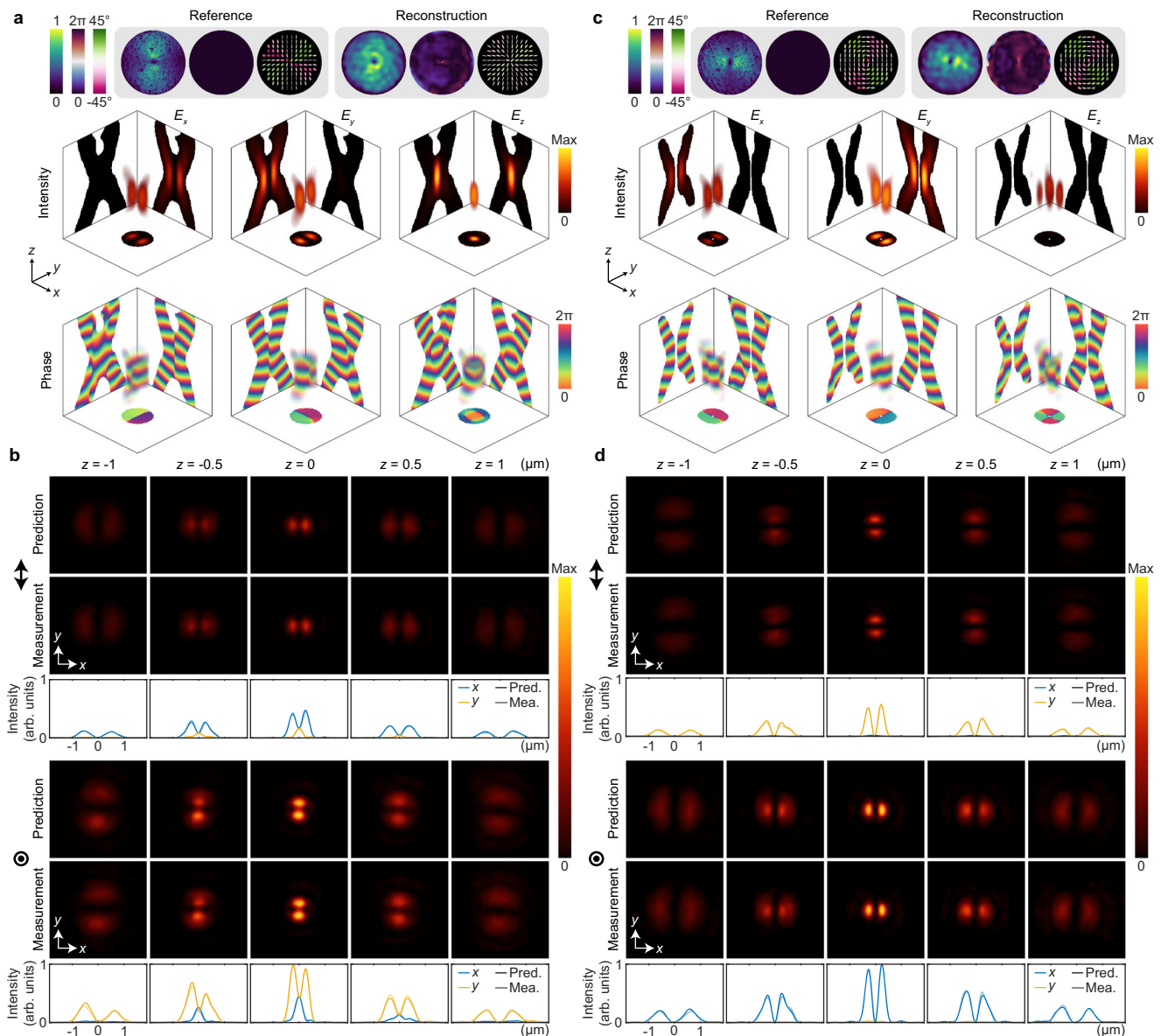


**Fig. 2 | Experimental results.** **a** The reference VPF (top left), the reconstructed ones (top right), and the reconstructed  $\text{PSF}_{\text{vec}}$  in 3D space with 2D projections (middle and bottom rows) for the radially polarized beam. For visualization purpose, only regions with significant intensity are shown in the tomography, with volume size  $(3.84 \mu\text{m})^3$ . **b** The predicted and measured two-channel PSFs without phase encoding at different depths for the radially polarized beam. The blue and

yellow lines indicate intensity profiles along the  $x$  and  $y$  directions, respectively. Opaque lines represent the predicted PSFs, while translucent lines represent the measured ones. The measured PSFs are processed by low-pass filtering with the objective's bandwidth since the raw data suffers from Poisson noise (Supplementary Section 5.4). **c**, **d** are for the azimuthally polarized beam.

### Application in field manipulation

Here we demonstrate that our method enables fully vectorial manipulation of the  $\text{PSF}_{\text{vec}}$  in situ using a gradient-based algorithm (Supplementary Sections 6.1–6.2). In previous works, the amplitude and phase of the  $\text{PSF}_{\text{vec}}$  can not be flexibly controlled<sup>36–41</sup>. In addition, the in situ manipulation remains missing. In contrast to these methods, we generate the desired  $\text{PSF}_{\text{vec}}$  in situ given the experimentally retrieved VPF. For this demonstration, we optimize the VPF's phase with the constraints of previously retrieved amplitude and polarization in Fig. 2. We adopted radial polarization because it offers sufficient  $E_z$  strength, which facilitates the 3D polarization manipulation.

We first generated an optical focus array with predefined 3D polarization states (Fig. 3a–c), where the optimized  $\text{PSF}_{\text{vec}}$  reaches 76% accuracy. Besides, the reconstructed VPF and  $\text{PSF}_{\text{vec}}$  further verify the optimized counterparts in experimental realization. The

dark areas in the VPF's amplitude are caused by phase singularities. Discrepancies in the reconstructed  $\text{PSF}_{\text{vec}}$  are attributed to the amplitude and polarization constraints of the VPF during optimization since they vary with the phase in experiments when involving high-frequency features.

To demonstrate our method on a more challenging target, we applied our method to continuous fields (Fig. 3d–f). Compared with discrete foci, continuous fields may possess more rapid spatial variations (Supplementary Section 6.3). Although the optimized  $\text{PSF}_{\text{vec}}$  shows a ring-shaped intensity similar to the target, we are aware of a noticeable deviation in the 3D polarization (21% accuracy). This phenomenon stems from phase-only modulation of the VPF. Better accuracy is possible if the modulation also includes amplitude and polarization. Nonetheless, the reconstructed VPF and  $\text{PSF}_{\text{vec}}$  experimentally verify the optimized ones. Notably, the optimization for field



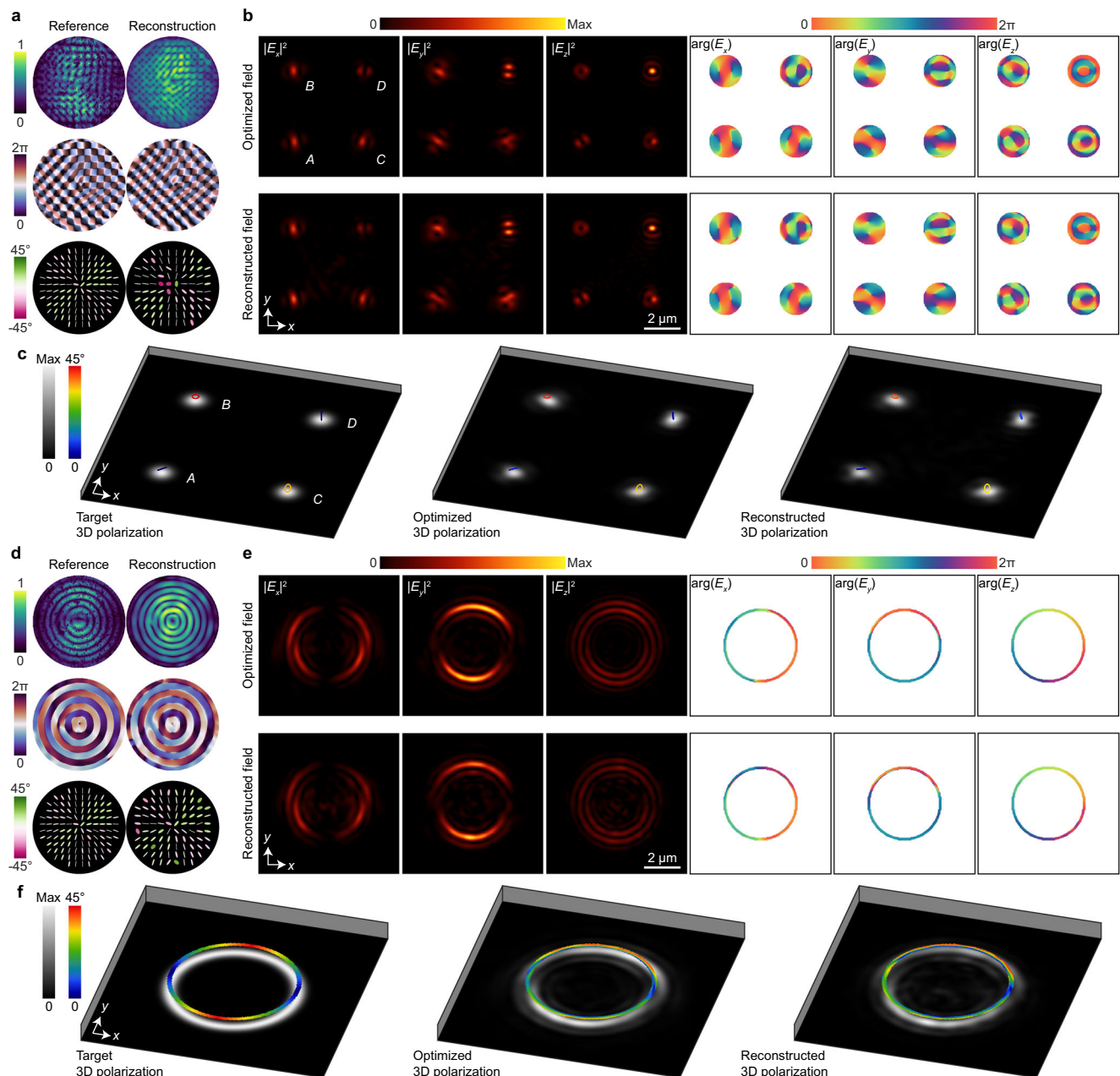


**Fig. 3 | Created complicated 3D polarization in situ.** **a** The reference VPF (left column), and the reconstructed one (right column). In the reference VPF, the middle row displays the phase optimized for the desired  $\text{PSF}_{\text{vec}}$ . The top row illustrates the amplitude captured by the Stokes camera when the optimized phase is loaded onto a spatial light modulator (SLM). The bottom row shows the polarization constraint applied during phase optimization. **b** The optimized  $\text{PSF}_{\text{vec}}$  (top row), and the reconstructed counterpart (bottom row). Only regions with significant intensity are shown in the phase visualization. The electric fields of the target four foci are  $\mathbf{E}_A = [1/\sqrt{2}, 1/\sqrt{2}, 0]^T$ ,  $\mathbf{E}_B = [1/\sqrt{2}, e^{i\pi/2}/\sqrt{2}, 0]^T$ ,  $\mathbf{E}_C = [1/\sqrt{3}, e^{-i\pi/2}/\sqrt{3}, 0]^T$ , and  $\mathbf{E}_D = [0, 0, 1]^T$ , respectively, where  $^T$  denotes matrix transpose. **c** The polarization and intensity of the target (left column), the optimized (middle column), and the reconstructed (right column)  $\text{PSF}_{\text{vec}}$ . The gray and rainbow colormaps indicate the intensity and the 3D polarization ellipticity, respectively. The normal directions of 3D polarization ellipses are omitted, as  $E_z$  may dominate. **d–f** are for continuous  $\text{PSF}_{\text{vec}}$ . The electric field of the target continuous field is  $\mathbf{E}(\mathbf{r}) = [\cos \varphi(\mathbf{r}), \sin \varphi(\mathbf{r}), e^{i\varphi(\mathbf{r})}]^T$ , where  $\mathbf{r}$  and  $\varphi$  represent the position vector and the azimuthal angle on the focal plane, respectively.

manipulation is faster (within 1 s) compared to reconstruction (within 10 s), due to a more constrained optimization target.

### Application in AO-assisted nanoscopy

In optical nanoscopy, adaptive optics (AO) allows for better resolution<sup>42</sup> by compensating for the aberrations at the objective's BFP. Our method demonstrates its applicability, particularly in stimulated emission depletion (STED) nanoscopy<sup>43</sup>. The standard AO-assisted STED nanoscopy involves either optimizing the phase

component of the VPF represented by Zernike polynomials using hill-climbing method<sup>44–46</sup>, which needs to capture nearly a hundred images, or employing Shack–Hartman wavefront sensor with increased system complexity<sup>47</sup>. These methods, which rely on the incomplete scalar model and fail to access the in situ VPF, prove useful to some extent. However, since a high-NA objective is of the essence in STED nanoscopy, further enhancement is limited. The VPF's phase can't be faithfully retrieved without considering its amplitude and polarization<sup>48,49</sup>, as well as the imperfections in the detection path. In

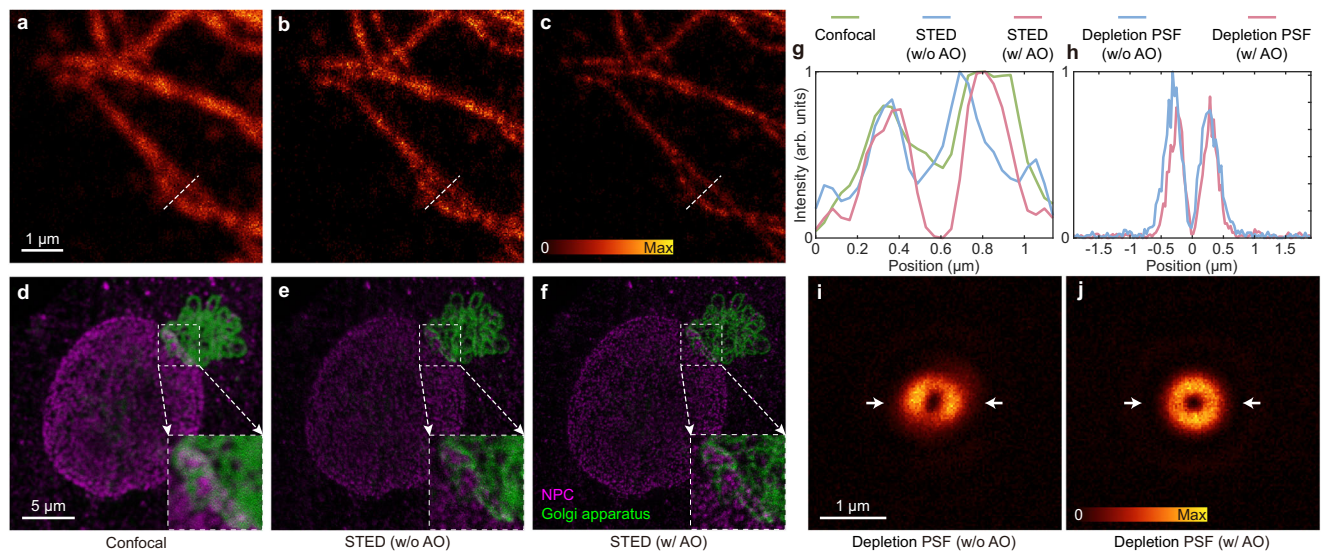


**Fig. 4 | STED imaging with in situ aberration correction.** **a–c** From left to right, these images show microtubules imaged using confocal microscopy, and STED nanoscopy without and with AO, respectively. Herein, the confocal image only serves as a rough reference to verify the STED images. **d–f** Two-color imaging results of the NPC and Golgi apparatus. **g** Intensity profiles along the white dashed

lines in (a–c), with slight smoothing applied for visualization. **h**, Intensity profiles along the arrows shown in (i, j). **i, j** are the measured PSFs of the depletion beam with and without AO, respectively. Data shown are representative samples from  $n = 5$  cells for (a–c) and (d–f).

contrast, as a more complete and accurate approach, ours harnesses AO better.

In our configuration, the depletion PSF was created by tightly focusing a circularly polarized vortex beam. With the in situ retrieved VPF, we achieved enhanced STED imaging by correcting the phase aberration. Specifically, aberration correction was realized by loading a conjugate counterpart of the retrieved phase aberration onto the SLM in the depletion path. During STED imaging, the fluorescence was detected by single-photon counting avalanche photodiodes. Notably, polarization split is not employed for fluorescence detection, because it only aims at recording the scattered signals from the nanoprobe to extract the phase aberration of the depletion beam. More details about the setup of the STED nanoscope and the imaging process can be found in our previous works<sup>46</sup>. In Fig. 4a–c, two adjacent microtubules are hardly distinguishable in confocal microscopy and STED nanoscopy without AO, but are clearly resolved after aberration correction. This improvement is further supported by their line profiles (Fig. 4g). As for the two-color imaging (Fig. 4d–f), the structures of the nuclear pore complex (NPC) and Golgi apparatus are also more clearly resolved with AO. These improvements originate from the more circular and hollow depletion PSF after aberration correction (Fig. 4i, j), which is further supported by the line profiles in Fig. 4h. More specifically, our method enhances the resolution of the microtubules and two-color imaging by ~15% and 25%, respectively, taking the images without AO for reference. The resolution is evaluated by decorrelation analysis<sup>50</sup>.

### Mixed-state problems

Mixed-state problems are ones for which the  $\text{PSF}_{\text{vec}}$  results from the incoherent and/or coherent superposition of multiple beams. Mixed-state problems are always complicated due to increased ambiguity and lower SNR (Supplementary Sections 7.1–7.2). While the demixing of scalar waves in low-NA systems is possible<sup>51,52</sup>, fully vectorial demixing in high-NA systems remains uncharted. Here we demonstrate the demixing of  $\text{PSF}_{\text{vec}}$  containing two states. Notably, we employed 20 pairs of phases for encoding with different distributions between the two states in each pair to alleviate the ambiguity.

We first present experimental results showing the demixing of an incoherent superposition of radially and azimuthally polarized beams

(Fig. 5a, b). These results match well independently reconstructed data shown in Fig. 2, reaching around 80% accuracy of the predicted two-channel PSFs without phase encoding. This accuracy is lower than that of single-state reconstruction (90%) since each state suffers from increased ambiguity and lower SNR.

Our method is also effective for coherent cases such as the  $\text{PSF}_{\text{vec}}$  created using a 4Pi microscope architecture<sup>53</sup> (Fig. 5c). The coherent utilization of two opposing objectives enhances the axial resolution in microscopy<sup>14,54</sup>. The simulated results are shown in Fig. 5d, where both the reconstructed  $\text{PSF}_{\text{vec}}$  and VPFs well reflect their ground truth with approximately 80% accuracy, including the phase difference between the two VPFs.

We can readily expand our ability of field manipulation in the single-objective architecture to the 4Pi one. For example, we repeated the design of a ring-shaped continuous pattern with a complicated 3D polarization, matching the target shown in Fig. 3f. Notably, this  $\text{PSF}_{\text{vec}}$  generated by 4Pi focusing (90% accuracy; see Supplementary Fig. S21) is more accurate than the result from one single objective (62% accuracy; see Supplementary Fig. S25). The 4Pi architecture offers double degrees of freedom and dramatically extends the bandwidth of the  $\text{PSF}_{\text{vec}}$  along the z-axis, enabling the creation of more intricate  $\text{PSF}_{\text{vec}}$ . Similarly, we present another demonstration with a more complicated 3D polarization structure with 88% accuracy. Notably, if polarization is not a priority, we can design the intensity distribution alone. For instance, using a single beam, we created an isotropic hollow PSF that potentially simplifies isoSTED nanoscope<sup>14</sup>. These results are provided in Supplementary Sections 7.5–7.7.

### Discussion

Our method attains reconstruction accuracy of roughly 90% in our configuration and 80% even amid substantial background noise. However, achieving higher accuracy remains contingent upon the SNR. To improve the signal level, it is advantageous to employ brighter probes and optimize the optical setup. Additionally, minimizing the refractive index mismatch in focal space can mitigate noise induced by laser reflection.

Our method requires a phase-modulation device for encoding. If incorporating such a device is impossible, mechanical defocus can

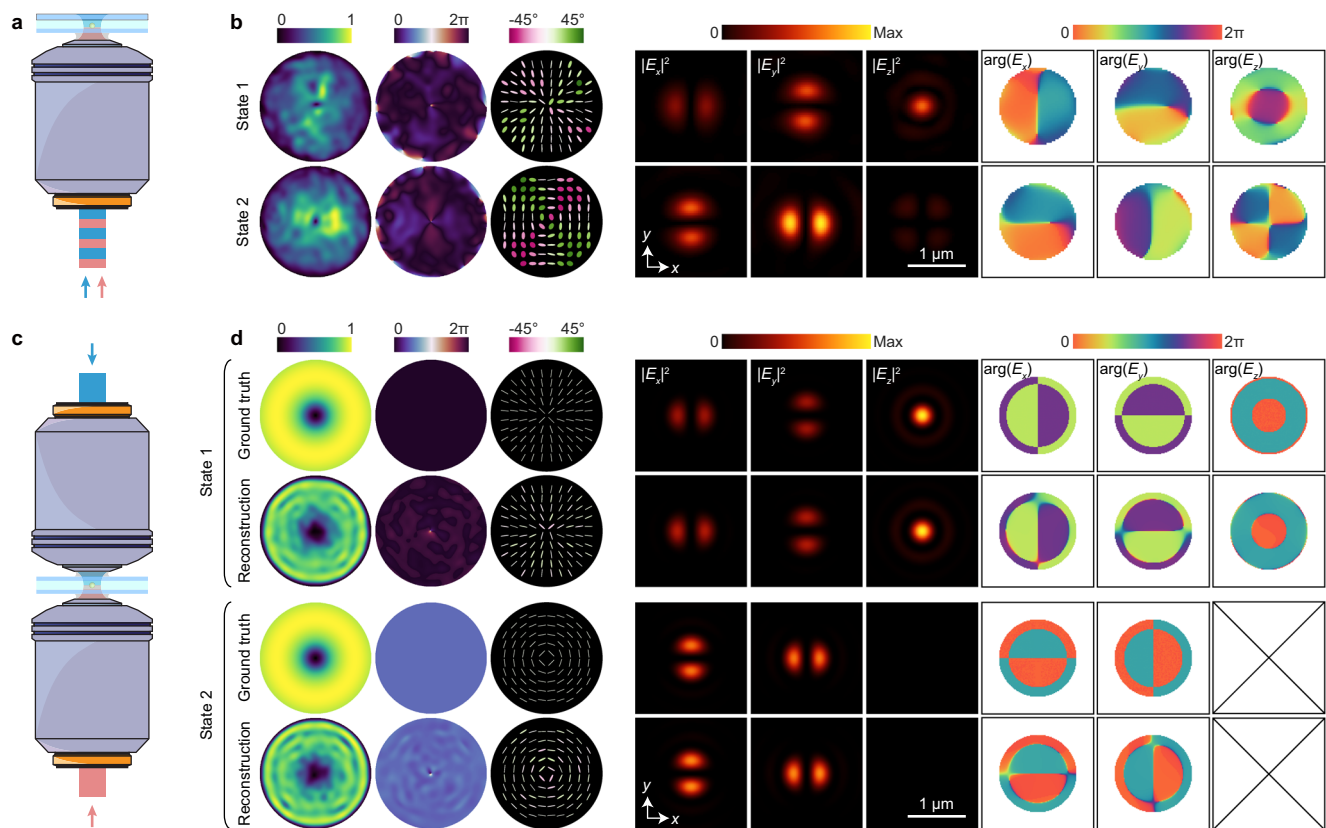


**Fig. 5 | Demixed results of two states.** **a** Schematic illustration of incoherent superposition. The red and blue colors denote different beams. **b** Experimental results for incoherent demixing. From left to right, the 1st–3rd columns denote the retrieved VPF; the 4th–6th and 7th–9th columns denote the intensity and phase of the reconstructed  $\text{PSF}_{\text{vac}}$ , respectively. The phase encoding of the two states is achieved by simultaneously modulating different regions on the SLM to impose two distinct phases<sup>46</sup>. **c** Schematic illustration of 4Pi focusing. In this configuration,

two counter-propagating beams interfere near the shared focus of two opposing objectives. The resulting coherent mixed state consists of radially and azimuthally polarized beams with a phase difference. **d** Simulated results for coherent demixing. From left to right, the 1st–3rd columns denote the VPF; the 4th–6th and 7th–9th columns denote the intensity and phase of the  $\text{PSF}_{\text{vac}}$ , respectively. In **(b, d)**, only the fields on the focal plane are shown (see Supplementary Sections 7.3 and 7.4 for their 3D distribution).

serve as an alternative. This alternative is simplified but risky, because it reduces the SNR and may fail to eliminate ambiguities.

In our experimental demonstrations of field manipulation and AO-assisted nanoscopy, we solely manipulated or corrected the VPF's phase. Further improvement is achievable by incorporating the VPF's amplitude and/or polarization (Supplementary Sections 8.1–8.2). Nevertheless, it requires a more complicated system at the expense of reduced light efficiency<sup>49</sup>.

Regarding temporal efficiency, our method needs to acquire 10 pairs of encoded PSFs for accurate reconstruction. In addition, the decoding algorithm takes several extra seconds for iteration. These requirements render our method insufficient for real-time applications. However, if the VPF's polarization is not intricate, appropriate scalar approximations significantly reduce processing time. For example, with just 5 phases for encoding, scalar reconstruction is completed in approximately 0.05 s, roughly 200 times faster than fully vectorial reconstruction (Supplementary Section 8.3). Further reduction in measurements and iterations could be achieved by integrating deep learning techniques<sup>55</sup>. Nevertheless, these alternatives compromise accuracy.

In summary, we have presented a method for in situ fully vectorial tomography and pupil function retrieval of  $\text{PSF}_{\text{vac}}$  from 2D encoded PSFs. Notably, the in situ capability of our method is based on the insight that the vectorial information of the original field is well-preserved in the encoded measurements, which has been confirmed by the accurate reconstruction in both simulations and experiments. By employing elaborately designed phase encoding in the focusing

path and splitting polarization in the detection path, our method effectively eliminates ambiguity. The fully vectorial information is then efficiently decoded using analytically derived gradients and matrix implementation of the Fourier transform with minimal samples. Our method is notably robust against aberrations, benefiting from the focus scanning strategy and decoding algorithm. We have demonstrated this method for in situ creating complicated 3D polarization structures and correcting aberrations in optical nanoscopy. Our method also proves applicable for resolving the mixed-state challenges.

Our development provides access to the properties of the electric field, a fundamental representation of light, at the nanoscale in practical deployment especially in point-scanning setups. It also represents an important step toward characterizing and optimizing more advanced parameters in experiments, such as energy flow, angular momentum, and optical force.

## Methods

### Phase design for encoding

Phase diversity can be achieved by defocus or vanilla random phase<sup>27,28,30</sup>. However, these methods often encounter challenges with limited diversity and low SNR. For accurate reconstruction, it is essential that the phases used for encoding are distinct enough to minimize ambiguity, while also ensuring that the PSFs remain within a confined FOV to maintain a high SNR.

Our phase design is informed by Fourier optics, specifically the relationship between the extension of the PSF and the spatial gradient



of the VPF's phase<sup>34</sup>. However, directly generating a phase with a specific gradient constraint is challenging. Therefore, we propose a solution that involves randomly generating two smooth matrices to represent the initial gradient distribution along the  $x$  and  $y$  directions, constrained within a specified range. It is crucial to account for the inherent phase gradient present in the VPF, which can cause the PSF to extend beyond the size of an aberration-free Airy disk. To address this, we exclude this intrinsic phase gradient, which is estimated beforehand from the initial PSF size without phase encoding. Assuming the initial PSF size is  $L_x \times L_y$ , and the target FOV is  $L_x \times L_y$ , the phase pattern is designed to expand the PSF along each axis by  $\Delta x = 0.5(L_x - l_x)$  and  $\Delta y = 0.5(L_y - l_y)$ , respectively. According to Fourier optics, the maximum allowable phase gradient is expressed as

$$\left| \frac{\partial \phi(k_x, k_y)}{\partial k_y} \right|_{\max} = \Delta y, \quad (2)$$

where  $y \in \{x, y\}$ .  $(k_x, k_y)$  are the coordinates in the BFP, represented by spatial frequency. With this gradient constraint, the phase for encoding is generated by solving an inverse gradient problem<sup>56</sup>.

### Experimental implementation

To realize our method, a point scanning microscope was used. A vectorial excitation beam was focused into the sample using a high-NA silicone immersion objective (NA = 1.35) and raster scanned to form an image. The designed random phase patterns were sequentially loaded onto a deformable mirror (DM) for encoding. The scattered light from a gold nanosphere was collected using the same objective, and then split into the p- and s-channels by rotating a linear polarizer. The p- and s-channels were directed onto a photomultiplier tube, and the intensities were recorded sequentially, which were then used to recover the VPF. Therefore, a pair of two-channel PSFs was recorded for each random phase pattern. Notably, before loading these random phase patterns onto the DM, they were decomposed into low-order Zernike polynomials. Subsequently, the coefficients of Zernike polynomials were used to control the DM<sup>46,57</sup>, considering its smooth representation capability. More information of our experimental setup can be found in Supplementary Fig. S12.

### Probe sample preparation

A gold nanosphere with a diameter of 150 nm was used as the probe. These gold nanospheres (A11-150-CIT-DIH-1-25, Nanopartz) were sparsely deposited onto a coverslip (CG15CH2, Thorlabs), and subsequently embedded in oil (IMMOIL-F30CC, Olympus). The coverslip was then fixed onto a glass slide using nail polish, which was allowed to cure for 24 h.

### Biological samples preparation

For microtubule labeling, U2OS (human osteosarcoma cell line) cells were purchased from the American Type Culture Collection and cultured in McCoy's 5A medium (Thermo Fisher Scientific) supplemented with 10% (v/v) FBS. The cells were maintained at 37 °C in a humidified 5% CO<sub>2</sub> environment and seeded into glass-bottom dishes (NEST Scientific) at a density of  $1.5\text{--}2.0 \times 10^4$  cells per well before labeling. Following overnight incubation, the cells were washed three times with phosphate-buffered saline (PBS; Thermo Fisher Scientific), fixed with 3% (m/v) paraformaldehyde (Electron Microscopy Sciences) and 0.1% (v/v) glutaraldehyde (Sigma-Aldrich) for 10 min at 37 °C, and then quenched with NaHB<sub>4</sub> for 7 min at room temperature (RT). The cells were subsequently incubated with 0.2% (v/v) Triton X-100 (Sigma-Aldrich) and 5% goat serum (Thermo Fisher Scientific) for 1 h at RT. Microtubules were stained with mouse anti- $\alpha$ -tubulin (AF2827; Beyotime Biotechnology) and mouse anti- $\beta$ -tubulin (AF2835; Beyotime Biotechnology) at 1:100 dilution in PBS overnight at 4 °C, and followed

by goat anti-mouse STAR RED (STRED-1001-500UG; Abberior GmbH) at 1:200 dilution in PBS for 1 h. Before imaging, the samples were washed three times with PBS for 3 min each.

NPC and Golgi apparatus samples (Cells 4C NPC-STAR RED; Golgi-STAR ORANGE; Actin-STAR GREEN; DAPI) were purchased from Abberior.

### Reporting summary

Further information on research design is available in the Nature Portfolio Reporting Summary linked to this article.

### Data availability

The data used to reproduce the results of this study are available from the corresponding authors upon request.

### Code availability

Customized code is available at <https://github.com/hao-laboratory/tightly-focused-field-tomography><sup>58</sup>.

### References

- Quabis, S., Dorn, R., Eberler, M., Glockl, O. & Leuchs, G. Focusing light to a tighter spot. *Opt. Commun.* **179**, 1–7 (2000).
- Wang, H. F., Shi, L. P., Lukyanchuk, B., Sheppard, C. & Chong, C. T. Creation of a needle of longitudinally polarized light in vacuum using binary optics. *Nat. Photon.* **2**, 501–505 (2008).
- Zhan, Q. Cylindrical vector beams: from mathematical concepts to applications. *Adv. Opt. Photon.* **1**, 1–57 (2009).
- Zhao, Y., Edgar, J. S., Jeffries, G. D. M., McGloin, D. & Chiu, D. T. Spin-to-orbital angular momentum conversion in a strongly focused optical beam. *Phys. Rev. Lett.* **99**, 073901 (2007).
- Man, Z., Xi, Z., Yuan, X., Burge, R. E. & Urbach, H. P. Dual coaxial longitudinal polarization vortex structures. *Phys. Rev. Lett.* **124**, 103901 (2020).
- Bauer, T. et al. Observation of optical polarization Möbius strips. *Science* **347**, 964–966 (2015).
- Maucher, F., Skupin, S., Gardiner, S. A. & Hughes, I. G. Creating complex optical longitudinal polarization structures. *Phys. Rev. Lett.* **120**, 163903 (2018).
- Zeng, Y., Yu, Y., Shen, X., Chen, J. & Zhan, Q. Tightly focused optical skyrmions and merons formed by electric-field vectors with prescribed characteristics. *Nanophotonics* **13**, 251–261 (2024).
- Béguin, J.-B. et al. Reduced volume and reflection for bright optical tweezers with radial Laguerre–Gauss beams. *Proc. Natl. Acad. Sci. USA* **117**, 26109–26117 (2020).
- Wu, Y.-J. et al. Controllable microparticle spinning via light without spin angular momentum. *Phys. Rev. Lett.* **132**, 253803 (2024).
- Li, Z., Allegre, O. & Li, L. Realising high aspect ratio 10 nm feature size in laser materials processing in air at 800 nm wavelength in the far-field by creating a high purity longitudinal light field at focus. *Light Sci. Appl.* **11**, 339 (2022).
- Grosche, S. et al. Towards polarization-based excitation tailoring for extended Raman spectroscopy. *Opt. Express* **28**, 10239–10252 (2020).
- Balzarotti, F. et al. Nanometer resolution imaging and tracking of fluorescent molecules with minimal photon fluxes. *Science* **355**, 606–612 (2017).
- Hao, X. et al. Three-dimensional adaptive optical nanoscopy for thick specimen imaging at sub-50-nm resolution. *Nat. Methods* **18**, 688–693 (2021).
- Herrera, I. & Quinto-Su, P. A. Measurement of structured tightly focused beams with classical interferometry. *J. Opt.* **25**, 035602 (2023).
- Quinto-Su, P. A. Interferometric measurement of arbitrary propagating vector beams that are tightly focused. *Opt. Lett.* **48**, 3693–3696 (2023).



17. Maluenda, D., Aviñoá, M., Ahmadi, K., Martínez-Herrero, R. & Carnicer, A. Experimental estimation of the longitudinal component of a highly focused electromagnetic field. *Sci. Rep.* **11**, 17992 (2021).
18. Martínez-Herrero, R. et al. Local characterization of the polarization state of 3D electromagnetic fields: an alternative approach. *Photonics Res.* **11**, 1326–1338 (2023).
19. Grosjean, T. et al. Full vectorial imaging of electromagnetic light at subwavelength scale. *Opt. Express* **18**, 5809–5824 (2010).
20. Bauer, T., Orlov, S., Peschel, U., Banzer, P. & Leuchs, G. Nanointerferometric amplitude and phase reconstruction of tightly focused vector beams. *Nat. Photon.* **8**, 23–27 (2014).
21. Yang, D., Hu, H., Gao, H., Chen, J. & Zhan, Q. Mie scattering nanointerferometry for the reconstruction of tightly focused vector fields by polarization decomposition. *Photonics* **10**, 496 (2023).
22. Neugebauer, M. et al. Geometric spin Hall effect of light in tightly focused polarization-tailored light beams. *Phys. Rev. A* **89**, 013840 (2014).
23. Fienup, J. R. Phase retrieval algorithms: a comparison. *Appl. Opt.* **21**, 2758–2769 (1982).
24. Kromann, E. B., Gould, T. J., Juetten, M. F., Wilhelm, J. E. & Bewersdorf, J. Quantitative pupil analysis in stimulated emission depletion microscopy using phase retrieval. *Opt. Lett.* **37**, 1805–1807 (2012).
25. Hieu Thao, N., Soloviev, O. & Verhaegen, M. Phase retrieval based on the vectorial model of point spread function. *J. Opt. Soc. Am. A* **37**, 16–26 (2020).
26. Vishniakou, I. & Seelig, J. D. Differentiable optimization of the Debye-Wolf integral for light shaping and adaptive optics in two-photon microscopy. *Opt. Express* **31**, 9526–9542 (2023).
27. Gutiérrez-Cuevas, R., Alemán-Castañeda, L. A., Herrera, I., Brasselet, S. & Alonso, M. A. Vectorial phase retrieval in super-resolution polarization microscopy. *APL Photon.* **9**, 026106 (2024).
28. Gonsalves, R. Phase diversity: math, methods and prospects, including sequential diversity imaging. *10677 SPIE Photonics Europe* (SPIE, 2018).
29. Wu, Y., Li, F., Willomitzer, F., Veeraraghavan, A. & Cossairt, O. WISHED: wavefront imaging sensor with high resolution and depth ranging. In *2020 IEEE International Conference on Computational Photography (ICCP)*, 1–10 (IEEE, 2020).
30. Wu, Y., Sharma, M. K. & Veeraraghavan, A. WISH: wavefront imaging sensor with high resolution. *Light Sci. Appl.* **8**, 1–10 (2019).
31. Fannjiang, A. Absolute uniqueness of phase retrieval with random illumination. *Inverse Probl.* **28**, 075008 (2012).
32. Chipman, R., Lam, W. S. T. & Young, G. *Polarized light and optical systems* (CRC press, 2018).
33. Liu, X. et al. Fast generation of arbitrary optical focus array. *Opt. Lasers Eng.* **162**, 107405 (2023).
34. Wei, H., Liu, X., Hao, X., Lam, E. Y. & Peng, Y. Modeling off-axis diffraction with the least-sampling angular spectrum method. *Optica* **10**, 959–962 (2023).
35. Youngworth, K. & Brown, T. Focusing of high numerical aperture cylindrical-vector beams. *Opt. Express* **7**, 77–87 (2000).
36. Urbach, H. P. & Pereira, S. F. Field in focus with a maximum longitudinal electric component. *Phys. Rev. Lett.* **100**, 123904 (2008).
37. You, S. et al. Iterative phase-retrieval method for generating stereo array of polarization-controlled focal spots. *Opt. Lett.* **40**, 3532–5 (2015).
38. Ren, H., Shao, W., Li, Y., Salim, F. & Gu, M. Three-dimensional vectorial holography based on machine learning inverse design. *Sci. Adv.* **6**, eaaz4261 (2020).
39. Abouraddy, A. F. & Toussaint, K. C. Three-dimensional polarization control in microscopy. *Phys. Rev. Lett.* **96**, 153901 (2006).
40. Chen, J., Wan, C. & Zhan, Q. Vectorial optical fields: recent advances and future prospects. *Sci. Bull.* **63**, 54–74 (2018).
41. Liu, X. et al. Generation of arbitrary longitudinal polarization vortices by pupil function manipulation. *Adv. Photon. Res.* **2**, 2000087 (2021).
42. Booth, M. J. Adaptive optical microscopy: the ongoing quest for a perfect image. *Light Sci. Appl.* **3**, e165–e165 (2014).
43. Blom, H. & Widengren, J. Stimulated emission depletion microscopy. *Chem. Rev.* **117**, 7377–7427 (2017).
44. Gould, T. J., Burke, D., Bewersdorf, J. & Booth, M. J. Adaptive optics enables 3D STED microscopy in aberrating specimens. *Opt. Express* **20**, 20998–1009 (2012).
45. Zdańkowski, P., Trusiak, M., McGloin, D. & Swedlow, J. R. Numerically enhanced stimulated emission depletion microscopy with adaptive optics for deep-tissue super-resolved imaging. *ACS Nano* **14**, 394–405 (2020).
46. Tu, S. et al. Accurate background reduction in adaptive optical three-dimensional stimulated emission depletion nanoscopy by dynamic phase switching. *ACS Photon.* **9**, 3863–3868 (2022).
47. Velasco, M. G. M. et al. 3D super-resolution deep-tissue imaging in living mice. *Optica* **8**, 442–450 (2021).
48. Hao, X., Kuang, C., Wang, T. & Liu, X. Effects of polarization on the de-excitation dark focal spot in STED microscopy. *J. Opt.* **12**, 115707 (2010).
49. He, C., Antonello, J. & Booth, M. J. Vectorial adaptive optics. *eLight* **3**, 23 (2023).
50. Descloux, A., Grussmayer, K. S. & Radenovic, A. Parameter-free image resolution estimation based on decorrelation analysis. *Nat. Methods* **16**, 918–924 (2019).
51. Thibault, P. & Menzel, A. Reconstructing state mixtures from diffraction measurements. *Nature* **494**, 68–71 (2013).
52. Attal, B. & O'Toole, M. Towards mixed-state coded diffraction imaging. *IEEE Transactions on Pattern Analysis and Machine Intelligence* 1–12 (IEEE, 2022).
53. Hell, S. & Stelzer, E. H. Properties of a 4Pi confocal fluorescence microscope. *J. Opt. Soc. Am. A* **9**, 2159–2166 (1992).
54. Liu, W. et al. Breaking the axial diffraction limit: a guide to axial super-resolution fluorescence microscopy. *Laser Photonics Rev.* **12**, 1700333 (2018).
55. Wang, K. et al. On the use of deep learning for phase recovery. *Light Sci. Appl.* **13**, 4 (2024).
56. Färneback, G., Rydell, J., Ebbers, T., Andersson, M. & Knutsson, H. Efficient computation of the inverse gradient on irregular domains. In *2007 IEEE 11th International Conference on Computer Vision*, 1–8 (IEEE, 2007).
57. Antonello, J. et al. Optimization-based wavefront sensorless adaptive optics for multiphoton microscopy. *JOSA A* **31**, 1337–1347 (2014).
58. Liu, X. Tightly focused field tomography. <https://doi.org/10.5281/zenodo.14997910> (2025).

## Acknowledgements

We thank Yu Wang, Dazhao Zhu, Chuankang Li, and Yuran Huang for fruitful discussions, and Xin Luo, Wenwen Gong, Wenli Tao, and Lu Yang for helping prepare samples, and Yunpeng Wang for helping with experiments. This work is funded by National Key R & D Program of China (2022YFB3206000), and Scientific and Technological Innovation Project of China Academy of Chinese Medical Sciences (CI2023C009YG).

## Author contributions

Xin L. conceived the project, developed the methodology, performed the simulations, and conducted the experiments. S.T. helped with the optical setup. S.T. and Yiwen H. helped with the experiments. Yubing H. helped with sample preparation. X.H. supervised the project. Xin L. and X.H. wrote the manuscript. Y.P., C.K. and Xu L. reviewed the manuscript.

## Competing interests

The authors declare no competing interests.

## Additional information

**Supplementary information** The online version contains supplementary material available at <https://doi.org/10.1038/s41467-025-58830-2>.

**Correspondence** and requests for materials should be addressed to Xu Liu or Xiang Hao.

**Peer review information** *Nature Communications* thanks Hyeonseung Yu and the other, anonymous, reviewer for their contribution to the peer review of this work. A peer review file is available.

**Reprints and permissions information** is available at <http://www.nature.com/reprints>

**Publisher's note** Springer Nature remains neutral with regard to jurisdictional claims in published maps and institutional affiliations.

**Open Access** This article is licensed under a Creative Commons Attribution-NonCommercial-NoDerivatives 4.0 International License, which permits any non-commercial use, sharing, distribution and reproduction in any medium or format, as long as you give appropriate credit to the original author(s) and the source, provide a link to the Creative Commons licence, and indicate if you modified the licensed material. You do not have permission under this licence to share adapted material derived from this article or parts of it. The images or other third party material in this article are included in the article's Creative Commons licence, unless indicated otherwise in a credit line to the material. If material is not included in the article's Creative Commons licence and your intended use is not permitted by statutory regulation or exceeds the permitted use, you will need to obtain permission directly from the copyright holder. To view a copy of this licence, visit <http://creativecommons.org/licenses/by-nc-nd/4.0/>.

© The Author(s) 2025